Journal of Magnetism and Magnetic Materials 596 (2024) 171981

Contents lists available at ScienceDirect

Journal of Magnetism and Magnetic Materials

journal homepage: www.elsevier.com/locate/jmmm

Effect of Gd^{3+} ion doping on structural, optical, magnetic and dielectric properties on superparamagnetic $Mg_{0.5}Zn_{0.5}Fe_{2-x}Gd_xO_4$ ($0 \leq x \leq 1$) nanoparticles synthesized via oleic acid assisted chemical co-precipitation method

Priya Boora [a,1], Rohit Ranga [a,1], Pallavi Saini [a], Vasundhara Madaan [a], Permender Singh [a], Krishan Kumar [a,*], Ashok Kumar [b,*]

[a] Department of Chemistry, Deenbandhu Chhotu Ram University of Science & Technology, Murthal, Sonepat-131039, Haryana, India
[b] Department of Physics, Deenbandhu Chhotu Ram University of Science & Technology, Murthal, Sonepat-131039, Haryana, India

ARTICLE INFO

Keywords:
Metal Oxide
Spinel Ferrites
Co-precipitation
Magnetic Properties
Optical properties

ABSTRACT

In the present study, different compositions having general formula $Mg_{0.5}Zn_{0.5}Gd_xFe_{2-x}O_4$, (x = 0, 0.025, 0.050, 0.075, 0.1) were synthesized using chemical co-precipitation method. The substitution of Gd^{3+} ions have exhibited profound impacts on the structural, morphological, magnetic, and optical parameters of Mg-Zn ferrites. Single-phase cubic spinel structure has been substantiated by X-ray diffractometer (X-ray diffraction, XRD) analysis for all compositions without any contamination peak. The values of the lattice constant and X-ray density both show an increasing trend when the Gd^{3+} ion concentration increases. (Fourier transformed infrared spectroscopy) FTIR spectra recorded in the mid-infrared region (4000–400 cm^{-1}) exhibit two main absorption bands associated with the O_h and T_d sites within the frequency range of 400–600 cm^{-1}. Morphological studies using (High-resolution transmission electron microscopy) HR-TEM analysis reveal agglomeration of nanoparticles and the average particle size lies between 8 and 9 nm. Maximum magnetization displays an erratic trend with increasing Gd^{3+} ion concentration, although both retentivity and coercivity decreases. The hysteresis curve for samples of differing ratios of Gd^{3+} ions demonstrated the superparamagnetic nature. Tauc's plot was employed to calculate the energy bandgap (E_g) of synthesized nanoparticles and E_g value were observed to decline from 3.563 eV to 3.521 eV with an increasing Gd^{3+} ion concentration. Impedance analyzer was used in the frequency range of 100 Hz–100 MHz to study dielectric properties at room temperature. The dielectric parameters declined as the frequency values increased. Due to lower values of dielectric parameters in Gd^{3+} ion doped Mg–Zn nano-ferrite, these materials are suitable in the fabrication of devices that need to operate at high frequencies such as switching memory storage devices. Moreover, these materials are appropriate for application in ferrofluids and medicinal treatments such as magnetic hyperthermia because of their low coercive field value.

1. Introduction

In the recent past, nano-magnetism has seen prodigious technological and scientific ameliorations. Owing to their distinctive and astounding magnetic, dielectric, and electrical properties such as minimal eddy current losses, high chemical steadiness, nanosized soft ferrites are of special importance to scientists and find potential uses in domains such as data storage, magnetic shielding, power generation, sensors and other fields [1–5]. The spinel ferrites having general formula MFe_2O_4 (M is any divalent cation, such as Zn^{2+}, Mg^{2+}, Mn^{2+}, Cd^{2+}, etc.) have a cubic closed-packing arrangement of O^{2-} ions with 32 octahedral interstitial sites (B-site) and 64 tetrahedral sites (A-site). Out of which M^{2+} and Fe^{3+} ions can occupy 16 octahedral (O_h) or 8 tetrahedral (T_d) sites [6]. Magnetic iron oxide nanoparticles (NPs) are being widely researched as therapeutic and diagnostic agents owing to their low cost, tunable characteristics, and biocompatibility. Improving the diverseness of nano ferrite mixtures and enhancing their structural and physical properties are two of the most vital study areas in this subject [7–9]. The

* Corresponding authors.
E-mail addresses: krishankumar.chem@dcrustm.org (K. Kumar), ashokkumar.phy@dcrustm.org (A. Kumar).
[1] Authors contributed equally

https://doi.org/10.1016/j.jmmm.2024.171981
Received 17 November 2023; Received in revised form 12 March 2024; Accepted 20 March 2024
Available online 21 March 2024

super-exchange interaction between magnetic ions at A and B sites causes ferrimagnetism in spinel ferrites. So, from both theoretical and an applied perspective, it is crucial to have a deeper knowledge of the magnetic, structural, and electrical characteristics of spinel ferrites. These ferrite material properties are frequently controlled by the method of synthesis, annealing temperature, time, conditions, and doping constituents into the A-site or B-site to alter the structural parameters and cation distribution [10].

Zinc ferrite ($ZnFe_2O_4$) is among commonly used spinels because of its non-toxic nature, high chemical stability, mild saturation magnetism, strong coercivity, and minimal band gap value [11]. Therefore, to attain outstanding characteristics, the $ZnFe_2O_4$ NPs are doped with diverse dopants using several techniques. Magnesium ferrite ($MgFe_2O_4$) is a complement to $ZnFe_2O_4$ in the electrical domains [12]. The lattice structures of these two ferrites differ between $MgFe_2O_4$ (inverse spinel) and $ZnFe_2O_4$ (normal spinel). As a result, the qualities of a mixed spinel lattice structure are paramount to normal spinel [13]. Numerous research teams from across the world have analyzed the electric and magnetic characteristics of Mg-Zn Nano ferrites (NFs) with various dopants. To analyze the magnetic and structural properties, Shinde and his group synthesized Mg-Zn ferrite powders of fixed composition via the oxalate co-precipitation method [14]. Reyes et. al explored the magnetic and structural parameters of Mg-Zn NFs synthesized using the sol–gel method. [15]. El Hiti investigated the dielectric behavior of Mg-Zn nano ferrites [16].

Researchers have expressed worries about mechanical strength, tangent loss, and physical stability despite the many features [17–19]. To overcome such fundamental issues, rare earth (RE) ions (Gd, Pr, Nd, Sm) doping in spinel ferrite NPs is done to enhance magnetic characteristics [20–22]. Introducing RE ions such as Ce^{3+}, La^{3+}, Tb^{3+}, Gd^{3+}, Ho^{3+} etc. into the spinel structure is said to cause structural distortion, create strain, and thereby enhance the electrical and magnetic properties [23,24]. Many researchers studied the outcome of Gd-doped spinel ferrites and reported remarkable shift in the characteristics of spinel ferrites. Jinka et. al reported the electrical and magnetic analysis of mixed Mg-Cd spinel ferrites with the doping effect of Gd^{3+} ions [25]. Kumar et. al studied the Gadolinium doped Zn-Ni ferrite's effects on impedance and transport phenomenon [26]. In their investigation Vani et al. reported a decrease in dielectric constant value for Co-ferrite nanoparticles on doping of Gd^{3+} ion suggesting the potential application for high-frequency devices [27].

The NPs produce localized heat when excited by an alternating current (AC) magnetic field, which can be used to treat malignant cancerous tissues or pathogenic bacteria with magnetic hyperthermia properties [28]. Biocompatibility of Mg-Zn ferrites and their utilization as a heat mediator in magnetic hyperthermia treatments have also received attention. The Mg-Zn ferrite's induction heating behavior requires precise control to be used for magnetic hyperthermia [29]. Few research papers are reported for rare-earth doped Mg-Zn mixed ferrite nanoparticles but no research paper is reported for Gadolinium doped Mg-Zn mixed ferrite nanoparticles. Due to Gadolinium's ion (Gd^{3+}) relatively higher magnetic moment than Fe^{3+} ion, magneto-crystalline anisotropy, and biocompatibility, it is employed as a dopant ion in the recent study [30]. The addition of trace amounts of RE (Gd^{3+}) ions to Mg-Zn ferrites can change their magnetic properties. The co-precipitation methodology is commonly employed for the synthesis of non-coercive superparamagnetic NPs, which are crucial for biomedical applications. As a result, a series of Gd-doped magnesium-zinc ferrite, having the molecular formula $Mg_{0.5}Zn_{0.5}Gd_xFe_{2-x}O_4$, (x = 0, 0.025, 0.050, 0.075, 0.1), (MZGD) were thus synthesized using co-precipitation approach, resulting in nanoparticles ranging from 9 to 11 nm and their magnetic measurement analysis shows the superparamagnetic nature of the synthesized samples, which make these materials a potential candidate for the preparation of stable ferrofluid. Also, the tangent loss of these materials is low and decreases with increasing Gd^{3+} ion concentration making these materials a potential candidate for microwave absorption applications.

2. Experimental study

2.1. Chemicals

Analytical grade chemical reagents were utilized for synthesizing MZGD NPs are $Mg(NO_3)_3{\cdot}6H_2O$ (Alfa Aesar, 99 %), $Zn(NO_3)_3{\cdot}6H_2O$ (Alfa Aesar, 99 %), $Fe(NO_3)_3{\cdot}9H_2O$ (Merk, 98 %), $Gd(NO_3)_3{\cdot}6H_2O$ (Sigma Aldrich, 99.9 %), oleic acid (Fisher Scientific, 65 %), and ammonia solution (Fisher Scientific, 25 %).

2.2. Preparation of ferrites

Stoichiometric amounts of $Mg(NO_3)_2{\cdot}6H_2O$, $Zn(NO_3)_2{\cdot}6H_2O$, $Fe(NO_3)_3{\cdot}9H_2O$, $Gd(NO_3)_3{\cdot}6H_2O$ were dissolved separately in 14 mL deionized water (DI) and then dissolved together to obtain a homogeneous mixture. The synthesized samples are codes as follows $Mg_{0.5}Zn_{0.5}Fe_2O_4$ (MZP), $Mg_{0.5}Zn_{0.5}Fe_{1.975}Gd_{0.025}O_4$ (MZGD2), $Mg_{0.5}Zn_{0.5}Fe_{1.95}Gd_{0.05}O_4$ (MZGD5), $Mg_{0.5}Zn_{0.5}Fe_{1.925}Gd_{0.075}O_4$ (MZGD7) and $Mg_{0.5}Zn_{0.5}Fe_{1.9}Gd_{0.1}O_4$ (MZGD10). Then, 12 mL of technical grade oleic acid was added as a surfactant with continuous stirring and set on a magnetic stirrer with a heating surface for 15 min followed by a dropwise addition of precipitating agent NH_4OH with continuous and vigorous stirring. The synthesized brown precipitates were kept at 90 °C for 1 h. After cooling the reaction mixture at room temperature, it was rinsed multiple times with deionized water and completely dehydrated at 100 °C. With the aid of mortar and pestle, the acquired loose powder was manually pulverized. The dried product was heated for 3 h at 500 °C. Fig. 1 displays the various process involved in the preparation of MZGD ferrite NPs and the reactions involved are mentioned in Fig. 2.

2.3. Characterization Techniques

The Rigaku-Ultima IV X-ray diffractometer (XRD) with in the angle range of 20°–70° with a scan rate of 2°/min and radiation of CuKα (λ = 1.5406Å) were used to record X-ray diffraction. FTIR spectra in the range of 400–4000 cm^{-1} was obtained using Fourier Transform-Infrared spectroscopy technique (Perkin Elmer FRONTIER model) by utilizing KBr pellets. Analysis of the surface and formation of spherical structures in the synthesized MZGD samples was validated with High resolution transmission electron microscopy (HR-TEM) (TECHNAI G-20). The optical characteristics of MZGD ferrites were carried out using UV–Vis. spectrophotometer (UV-3600i Plus). The Vibrating Sample Magnetometer (VSM: Lakeshore model 7410S) instrument was employed to study the magnetic properties. Moreover, an impedance analyzer (WAYNE KERR 6500B) was employed to evaluate dielectric and impedance studies at room temperature within the frequency range of 100 Hz–100 MHz.

3. Results and discussion

3.1. X-ray diffraction study

To investigate the crystallite size, phase, and lattice characteristics of MZGD ferrite NPs, XRD was employed. The XRD pattern for MZGD NPs is shown in Fig. 3. The peak with maximum intensity (3 1 1) was used to estimate the values of lattice constant (a), the crystallite size (D), and interplanar spacing (d). The crystallite size (for all indexed peaks) of $Mg_{0.5}Zn_{0.5}Gd_xFe_{2-x}O_4$ is determined by using Debye- Scherrer's equation (Eq. (1) [31]:

$$D = \frac{K\lambda}{\beta cos\,\theta} \tag{1}$$

where λ denotes the wavelength of X-ray used (λ = 1.5406 Å), β

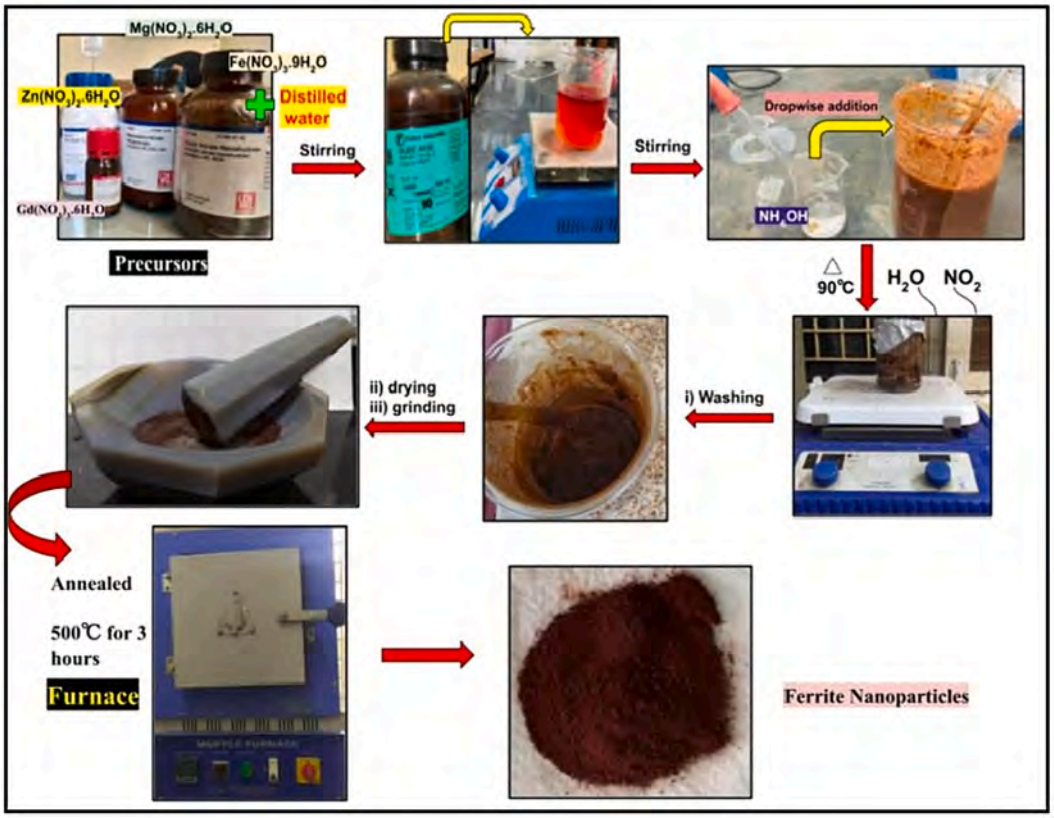

Fig.1. Schematical illustration for the synthesis of MZGD nano ferrites via Co-precipitation method.

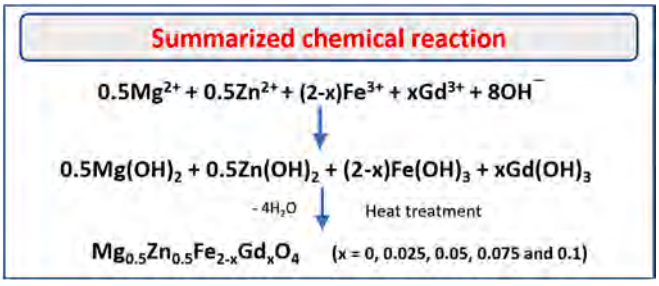

Fig.2. Chemical reactions involved in the synthesis of MZGD ferrite nanoparticles.

represents the values of full width at half maxima (in radians), K is known as Scherrer constant and its value taken in this study is 0.9 and θ is the diffraction or Bragg's angle. The values of lattice constant (a), and inter-planar spacing (d) included in Table 2 are computed using the Eqs. (2) and (3) mentioned below:

$$n\lambda = 2dsin\,\theta \tag{2}$$

$$a = d\sqrt{h^2 + k^2 + l^2} \tag{3}$$

where, h, k, and l represent the Miller indices of the diffracted plane.

Table 1 depicts the variations in lattice parameter (a) and crystallite size (D) values as Gd^{3+} ion concentration increases, and the variation is depicted in Fig. 4. The lattice constant values show an increasing trend when the Gd^{3+} ion concentration increases although with not much deviation, as shown in Table 1. Increasing values of lattice parameter can be attributed to the discrepancy between the ionic radii of Fe^{3+} and Gd^{3+} ions. Gd^{3+} ions, which have a larger ionic radius (0.094 nm), replace Fe^{3+} ions, which have a smaller ionic radius (0.067 nm). This

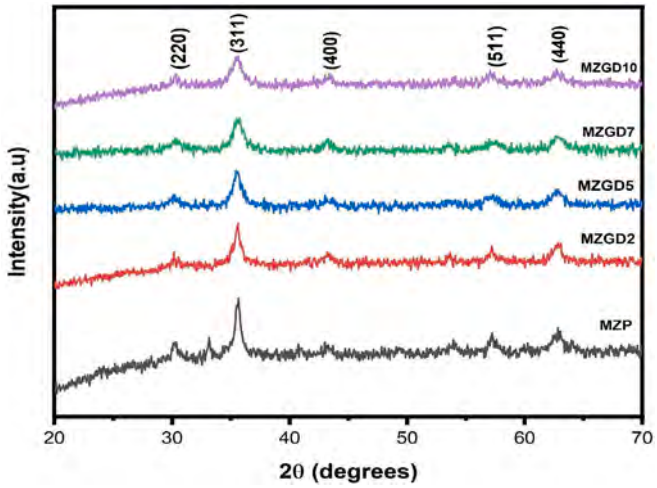

Fig.3. XRD pattern of MZP, MZGD2, MZGD5, MZGD7, and MZGD10 ferrite NPs.

causes unit cell distortion and lattice changes as a consequence of internal stress, which explains the increment of lattice constant values. Furthermore, increasing the Gd^{3+} ions concentration causes an inherent tension that deforms the spinel lattice and expands the unit cell. A similar trend of increasing lattice constant values with RE inclusion has also been supported in the literature [32,33].

The Eq. (4) was used to calculate the X-ray density (p_{XRD}) for undoped and doped ferrite samples [34,35], and Table 1 illustrates how density varied with Gd^{3+} ions concentrations.

$$\rho XRD = \frac{8M_w}{N_A a^3} \tag{4}$$

Table 1
Interplanar spacing (d), crystallite size (D), volume (V), lattice parameter (a), X-ray density (ρ_{XRD}), and strain (S_t) and crystallite size D_{W-H} using W–H plot for MZGD ferrite NPs.

Sample Composition	D (nm)	d (Å)	a (Å)	ρ_{XRD} (g/cm^3)	V (Å)^3	S_t x 10^{-3}	D_{W-H} (nm)
MZP	12.97	0.2520	8.358	4.91	583.89	2.26	11.60
MZGD2	10.91	0.2522	8.367	5.05	585.83	2.12	13.50
MZGD5	8.69	0.2524	8.371	5.14	586.62	1.28	8.08
MZGD7	9.10	0.2524	8.371	5.16	586.68	1.61	7.92
MZGD10	7.77	0.2525	8.376	5.30	587.76	1.94	8.95

Table 2
Cationic distribution in MZP, MZGD2, MZGD5, MZGD7, and MZGD10.

Composition	Cation distribution
MZP	$(Zn_{0.5}Mg_{0.05}Fe_{0.45})$ $[Mg_{0.45}Fe_{1.55}]$
MZGD2	$(Zn_{0.5}Mg_{0.05}Fe_{0.45})$ $[Mg_{0.45}Fe_{1.525}Gd_{0.025}]$
MZGD5	$(Zn_{0.5}Mg_{0.05}Fe_{0.45})$ $[Mg_{0.45}Fe_{1.5}Gd_{0.05}]$
MZGD7	$(Zn_{0.5}Mg_{0.05}Fe_{0.45})$ $[Mg_{0.45}Fe_{1.475}Gd_{0.075}]$
MZGD10	$(Zn_{0.5}Mg_{0.05}Fe_{0.45})$ $[Mg_{0.45}Fe_{1.45}Gd_{0.1}]$

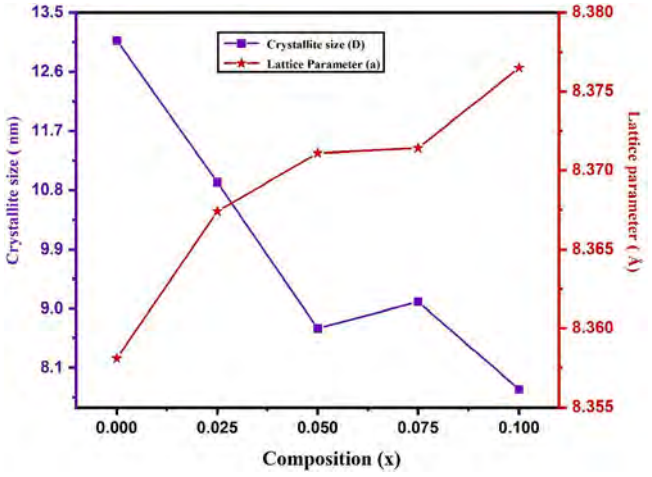

Fig.4. Composition-dependent behavior of lattice constant (a) and crystallite size (D) of MZGD ferrite NPs.

where 'N_A' is Avogadro's number (6.0225 x 10^{23} atoms/mole) and M_w is the molecular weight of the sample and 'a' is lattice constant [1]. X-ray density values increases linearly with Gd^{3+} ions concentration as iron atom has smaller ionic radii than gadolinium ions, a similar trend was found in the literature [2].

Williamson-Hall (W–H) plot was utilized to study X-ray peak broadening, which serves as the basis for the calculation of crystallite size and lattice strain in MZGD ferrite using a customized Scherrer's formula [36]. The widening of the peak caused by lattice strain (S_t) and crystallite size (D_{W-H}) may be calculated with the help equations Eqs. (5) and (6), and the results are presented in Table 1 [37,38]:

$$\beta_{hkl} = \beta_D + \beta_S = 4\varepsilon \tan\theta + \frac{0.9\,\lambda}{D_{W-H}\cos\theta_{hkl}} \tag{5}$$

$$\beta_{hkl} D_{W-H} \cos\theta = \frac{0.9\,\lambda}{4\varepsilon \sin\theta_{hkl}} \tag{6}$$

$\beta\cos\theta$ as the y-axis and $4\sin\theta$ as the x-axis were plotted on the W–H plots to estimate the values of crystallite size and strain. Hence, the fitted straight line's slope indicates the lattice strain in the sample, and the y-intercept was used to calculate crystallite size. The W–H plots in Fig. 5 display positive slopes for all compositions, which denotes the presence of tensile strain in the lattice and particle elongates as a result of this tensile strain indicating that these materials have strain [39,40].

The study of cation distribution offers a way to synthesize materials with desirable characteristics that can be used for wide range of applications [41]. Mohammed et. al presented the cation distribution for the MZP sample [42]. RE ions prefer the octahedral position by substituting the Fe^{3+} ion at B-site. Table 4 highlights the proposed cation distribution:

The following relations Eqs. (7) and (8) are employed to estimate the ionic radius at A and B sites using the cation distribution mentioned above:

$$r_A = (0.05r_{Mg} + 0.5r_{Zn} + 0.45r_{Fe}) \tag{7}$$

$$r_B = \frac{[0.5r_{Mg} + (1.55 - x)r_{Fe} + x.r_{Nd}]}{2}, 0 \le x \le 0.1 \tag{8}$$

where, x is the doping concentration of Gd^{3+} ions i.e., $0 \le x \le 0.1$, r_{Mg} (0.66 Å), r_{Gd} (0.94 Å), r_{Zn} (0.82 Å), and r_{Fe} (0.67 Å) are the ionic radius of Mg, Gd, Zn, and Fe respectively. The expansion of the O_h sites is driven by the doping of Gd^{3+} ions which leads to an increase in r_B. The estimated structural parameters ionic radii (r_A, r_B), oxygen position parameter (u), and theoretical lattice parameter (a_{th}) are shown in Table 3. Using the following formula Eqs. (9) and (10), u and a_{th} are calculated [43]:

$$u = \left(\frac{1}{a\sqrt{3}}(r_A + R_0) + \frac{1}{4}\right) \tag{9}$$

$$a_{th} = \frac{8}{3\sqrt{3}}[(r_A + R_0) + \sqrt{3}(r_B + R_0)] \tag{10}$$

where R_0 is the oxygen ion radius (1.32 Å).

There are various physical and chemical parameters that affect the oxygen position parameter (u). In spinel ferrites, the ideal 'U' value is 0.375 Å. The experimentally calculated value of 'u' is about 0.392 Å, suggesting that O^{2-} ions are in cubic closed packing (ccp) arrangement. The estimated values of u are observed to be higher than the ideal value demonstrating a change in chemical composition by doping, which provides an explanation behind the crystal lattice's deviation from the ideal spinel ferrite [44]. The hopping lengths (L_A, L_B) represent the separation between the magnetic ions at the T_d and O_h sites and were calculated using the formulas Eqs. (11) and (12) mentioned below and the results are summarized in Table 3 [32]:

$$L_A = \frac{a\sqrt{3}}{4} \tag{11}$$

$$L_B = \frac{a\sqrt{2}}{4} \tag{12}$$

It is observable that both L_A and L_B increase with increasing Gd^{3+} ion doping concentration. This trend in hopping length is directly related to values of lattice parameter. This variation could be attributed by the fact that the constituent ions' ionic radii differ, which leads the magnetic ions to come closer to one another and the hopping length to increase [45]. The inter-ionic cation–anion distance i.e., bond lengths at the T_d sites (R_A) and O_h sites (R_B) can be estimated with the help of the Eqs. (13)–(15) [46]:

$$R_A = a\sqrt{3}\left(\delta + \frac{1}{8}\right) \tag{13}$$

$$R_B = a\sqrt{3\delta^2 - \frac{\delta}{4} + \frac{1}{16}} \tag{14}$$

$$\delta = u - U \tag{15}$$

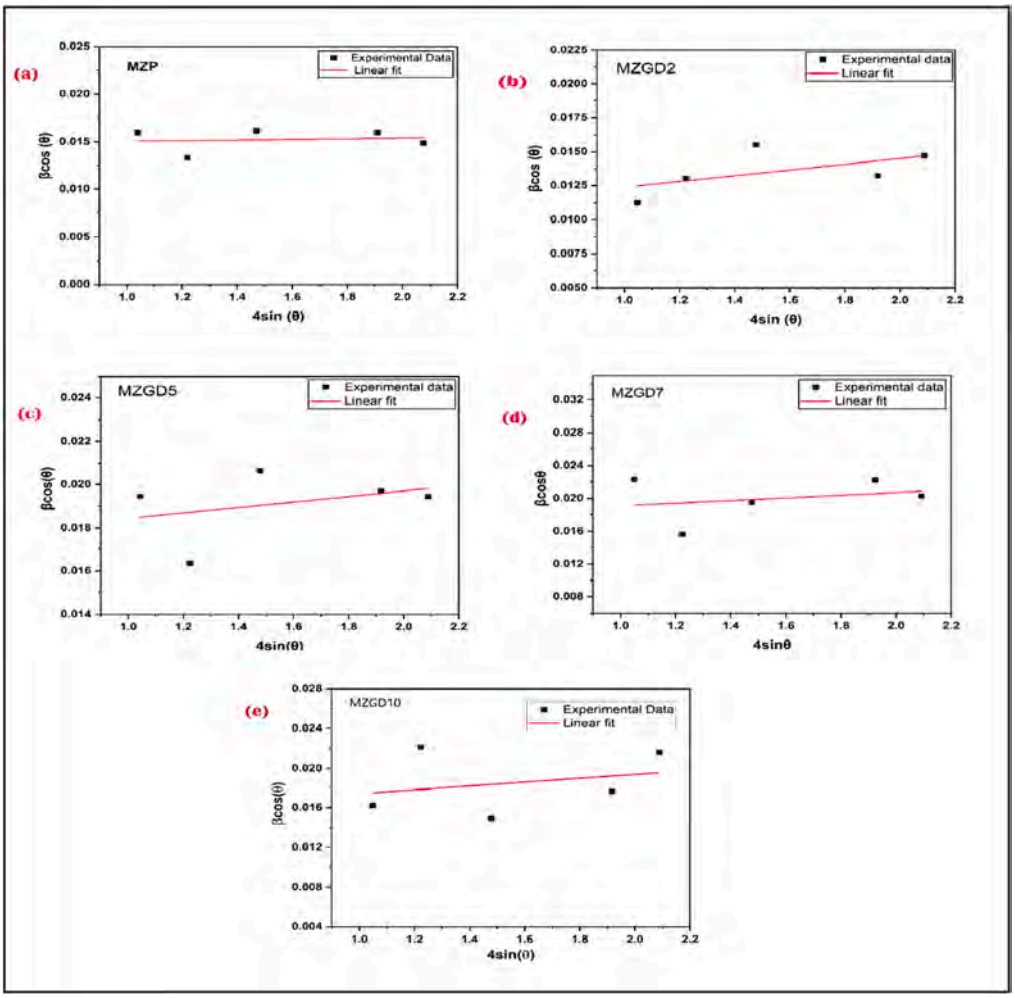

Fig.5. (a-e): W–H plots for MZGD ferrite NPs.

Table 3
Values of ionic radius (r_A, r_B), theoretical lattice parameter (a_{th}), oxygen position parameter (u), hopping lengths (L_A, L_B), Bond length (R_A, R_B), T_d shared edge (R_X), O_h edge (R_x'), and unshared O_h edge length (R_x'') of MZGD nano ferrites.

Composition	r_A (Å)	r_B (Å)	a_{th} (Å)	u (Å)	L_A (Å)	L_B (Å)	R_A (Å)	R_B (Å)	R_x (Å)	R_x' (Å)	R_x'' (Å)
MZP	0.7445	0.6678	8.4793	0.39261	3.6192	2.9550	2.06446	3.49867	3.37083	2.5383	2.9697
MZGD2	0.7445	0.6711	8.4883	0.39245	3.6232	2.9583	2.06443	3.50359	3.37080	2.5450	2.9727
MZGD5	0.7445	0.6745	8.4973	0.39239	3.6248	2.9596	2.06448	3.50553	3.37087	2.5475	2.9739
MZGD7	0.7445	0.6779	8.5063	0.39238	3.6429	2.9597	2.06441	3.50572	3.37075	2.5478	2.9740
MZGD10	0.7445	0.6813	8.5153	0.39230	3.6271	2.9615	2.06450	3.50837	3.37091	2.5513	2.9757

where δ is a deviation from the ideal oxygen parameter i.e., U=0.375 Å. The smallest distance between an oxygen ion and an A-site cation or B-site cation is known as R_A or R_B. Table 3 illustrates how the Gd^{3+} ion doping concentration affects the bond lengths R_A and R_B. The calculation of T_d edge (R_x), O_h shared edge (R_x'), and unshared O_h edge (R_x'') of the synthesized mixed spinel ferrites has been determined from the relation Eqs. (16)–(18) and are tabulated in Table 3 [47]:

$$R_x^{'} = a\sqrt{2}(1-2u) \tag{16}$$

$$Rx^{''} = a\sqrt{4u^2 - 3u + \frac{11}{16}} \tag{17}$$

$$R_x = a\sqrt{2}(2u-0.5) \tag{18}$$

The values of R_A and R_B ranges from 2.0645 Å to 3.5083 Å. Whereas shared and unshared edge values decreased with Gd^{3+} ion concentration and lie in the range from 3.5083 Å to 2.5383 Å [48]. The nature of metal ions and 'u' both are among the important factors responsible for these variations in all the parameters.

3.2. FTIR Analysis

It is possible to explain the existence of various bonds in a crystalline structure using FTIR spectroscopy. At room temperature (RT), the FTIR spectrum of $Mg_{0.5}Zn_{0.5}Fe_{2-x}Gd_xO_4$ ferrite NPs was observed in the 400–4000 cm^{-1} wavenumber range. The FTIR spectra in Fig. 6 for the synthesized MZGD ferrite samples show two prominent bands between 400 and 600 cm^{-1}, 445–452 cm^{-1} is the region of low-frequency band (ν_2) while the high-frequency band (ν_1) lies in the region 562–571 cm^{-1}.

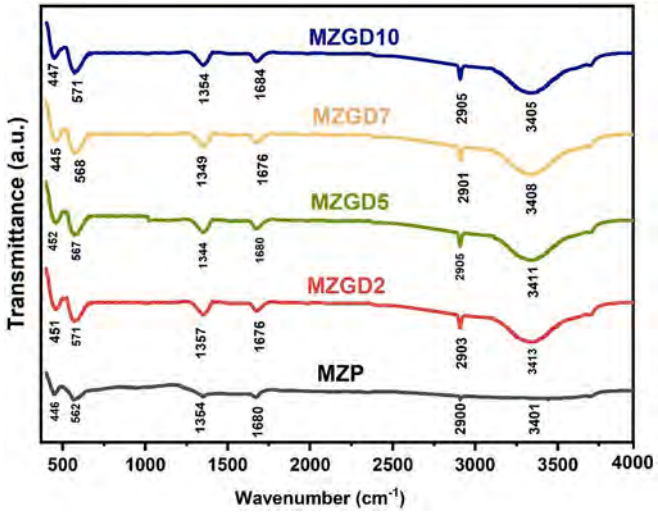

Fig.6. FTIR spectra of MZP, MZGD2, MZGD5, MZGD7, and MZGD10 ferrite NPs.

These vibration bands are usual properties of spinel ferrites [49]. A higher frequency drop (ν_1) at the T_d site represents the stretching vibrations occurring in the metal–oxygen bond, whereas (ν_2) at the O_h site represents the same vibration at a lower region of frequency. The increased frequency value of ν_1 is due to the distortion in lattice and the breakage of the metal–oxygen (Fe^{3+}–O^{2-}) bond by Gd^{3+} ions [50].

The peak near 1680 cm^{-1} belongs to N-O stretching, while that observed around 2905 cm^{-1} refers to C-H stretching [51]. The possible explanation for the shift in the values of ν_1 and ν_2 is because of crystal deformation by the inclusion of Gd^{3+} ions [52]. Moreover, due to changes in the crystalline field effect and strain in the lattice caused by the inclusion of Gd^{3+} ions, the position of peaks and intensity of these stretching modes vary with Gd^{3+} ion concentration. In addition to the peaks mentioned above the spectra in Fig. 6 shows broad humps due to asymmetric and symmetric stretching of water molecules, with maxima at about 3400 cm^{-1} [53]. The Eqs. (19) and (20) yield the force constant values of metal–oxygen bond at T_d and O_h sites and are listed in Table 4 [54]:

$$F_T = 4\pi^2 c^2 \nu_1^2 \mu \tag{19}$$

$$F_O = 4\pi^2 c^2 \nu_2^2 \mu \tag{20}$$

where μ is the reduced mass of Fe^{3+} and O^{2-} ions, c represents the speed of light (2.99 x10^{10} cm/s), and FTIR modes (ν_1 and ν_2) represent the vibrational frequency at A and B sites respectively.

3.3. HR-TEM analysis

The morphology of the MZGD nano-ferrites seen in Fig. 7(a and b) has been determined using HR-TEM. From the figure, it is apparent that particles shape is spherical and are narrowly distributed. Doping of Gd^{3+} ions alter the grain nucleation and crystal development of ferrite NPs. Ferrite nanoparticles agglomerate as a result of the addition of the Gd^{3+} ion which can be attributed to the magnetic interactions arising between the ferrite NPs.

Fig. 7(a and b) demonstrates the HR-TEM images for MZGD7 and MZGD10 and the average crystallite size for these compositions is calculated to be around 9 nm and 8 nm respectively. Fig. 7(c and d) represents two histograms plotted to highlight particle size distribution for MZGD7 and MZGD10. These results agree well with the results estimated using XRD measurements. The average crystallite size is discovered to be consistent with HR-TEM findings.

Table 4
Values of FTIR modes and force constants of MZFGD ferrite NPs.

Composition	Wave number ν_1 (cm^{-1})	Wave number ν_2 (cm^{-1})	F_T x 10^5 (Dynes/cm)	F_O x 10^5 (Dynes/cm)
MZP	562	446	2.315	1.458
MZGD2	571	451	2.390	1.491
MZGD5	567	452	2.356	1.497
MZGD7	568	445	2.365	1.451
MZGD10	571	447	2.390	1.465

3.4. UV–Vis. Spectra analysis

Optical study was done by collecting "Ultraviolet–visible NIR (UV–Vis.)" absorbance data in the region of 200–700 nm. Fig. 8 shows the absorption spectra of the synthesized sample. As observed in Fig. 8 the strength of absorption is intense, initially and gradually decreases as the wavelength increases until it nearly reaches saturation at the end (almost no absorption).

The alterations in energy bandgap (E_g) values of Gd^{3+} ion-doped Mg-Zn NFs were studied using Tauc's plots displayed in Fig. 9. The Tauc's plot [$(\alpha h\nu)^2$ v/s ($h\nu$)] was plotted using the UV–Vis absorbance data. Fig. 9 shows that as the Gd^{3+} ions doping level in Mg-Zn ferrites increased, values of energy bandgap steadily decreased from 3.563 eV to 3.521 eV. The undoped Mg-Zn ferrite has the highest band gap value. This was shown to be the case because of orbital overlapping within the Fe-3d and O2p energy states. However, the value of the band gap decreases when Gd^{3+} ions are doped into the lattice because the 4f energy levels of Gd^{3+} ions lie below the conduction band. The interaction between these energy levels of 4f and the O 2p orbital in the valence state causes the charges to relocate from the energy levels of Gd^{3+} ions to the conduction band of Mg-Zn ferrite NPs [55,56]. The variation of band gap with the composition of Gd^{3+} ions is depicted in Fig. 10.

3.5. Magnetic measurements

Room temperature VSM measurements were carried out to analyze the magnetic characteristics for various concentrations of MZGD ferrite NPs. The S-shaped hysteresis loops revealed the superparamagnetic nature of the synthesized samples. This observation can be attributed to the very small crystallite size of synthesized samples [57].

Fig. 11 depicts the hysteresis loop of synthesized samples. Table 5 lists the magnetic parameters that were determined from the hysteresis loop: maximum magnetization (M_{max}), coercivity (H_c), and magnetization remanence (M_r). Magnetic moment of the samples is calculated by using Eq. (21).

$$\mu_B = \frac{M.W \times M_{max}}{5585} \tag{21}$$

where, 5585 is the magnetic factor and *M.W* represents the molecular weight of samples. The values of magnetic moment are found to decrease with increasing Gd^{3+} ion concentration except for MZGD2 sample. This is resulted because at B sites, Gd^{3+} ions with greater magnetic moment (7.94B.M) replaces the Fe^{3+} ions which comparatively have lower magnetic moment (5.9B.M). RE metals exhibit substantial spin–orbit coupling of angular momentum in addition to having unpaired electrons in their 4f-shells. Furthermore, the $5s^25p^6$ orbital shields the 4f shell of rare-earth ions, which is nearly unaffected by the crystal field of the surrounding ions [58]. It is well acknowledged that the reason behind increasing coercivity is the resistance of domain wall displacement, which is affected by the microstructure. The movement of the domain wall may be restricted by the pores on grain boundaries. Hence, the coercivity of MZGD ferrite NPs is lower than the pure sample [59]. Except for MZGD2 and MZGD10 composition, the measured value of maximum magnetization (M_{max}) is observed to decrease with increasing Gd^{3+} ion doping. This is because rare earth ions have a low

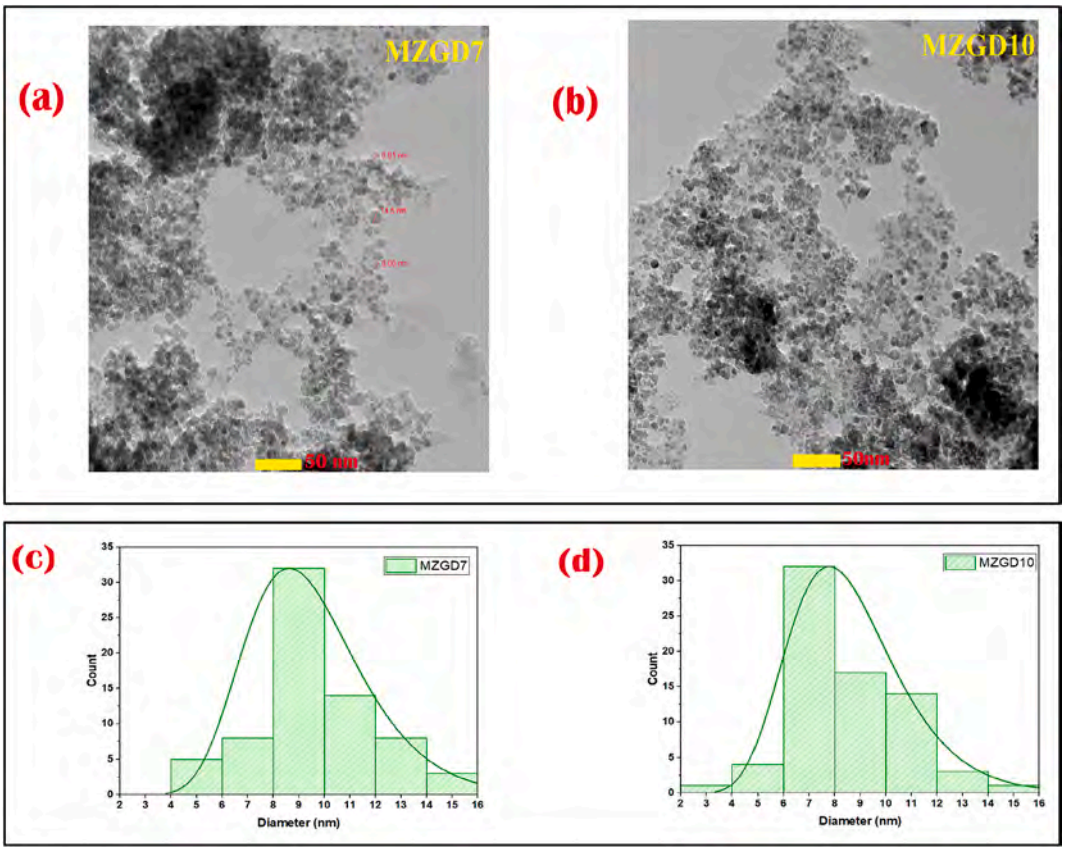

Fig.7. (a,b): HRTEM micrographs of MZGD7 and MZGD10; (c,d) particle size distribution of MZGD7 and MZGD10.

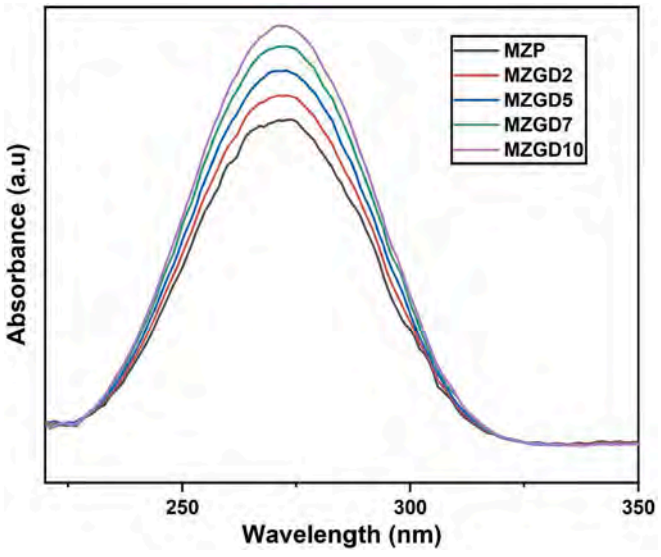

Fig.8. UV–Vis. spectra of the synthesized MZP, MZGD2, MZGD5, MZGD7, and MZGD10 ferrite NPs.

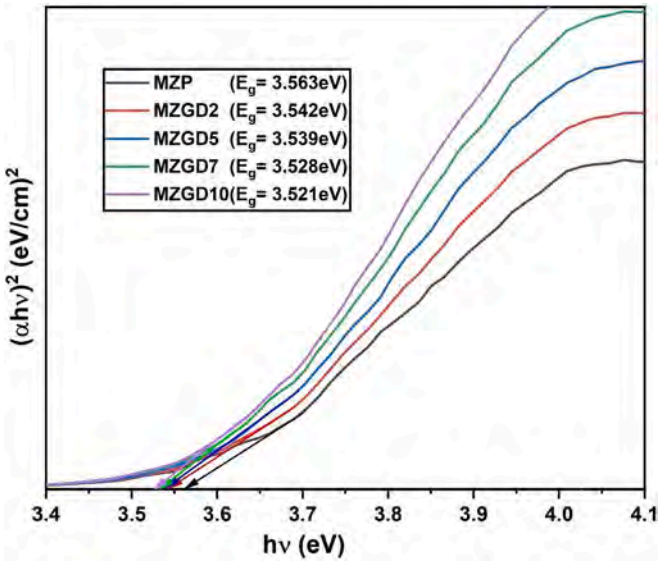

Fig.9. Tauc's plot for MZP, MZGD2, MZGD5, MZGD7, and MZGD10 ferrite NPs.

solubility, which causes the Gd^{3+} ions to move toward the grain boundary and raise the M_{max} value. The magnetic properties decreased with RE cation substitution, and similar findings were confirmed in our investigation except for MZGD2 and MZGD10 samples. It may be the result of Fe^{3+} ions being replaced by Gd^{3+} ions. Strain and lattice distortion brought on by the cation distribution could be responsible for the decrease in magnetization remanence (M_r) and coercivity (H_c) values [60]. The fluctuation in the values of H_c and M_{max} with the composition of MZGD ferrite NPs is shown in Fig. 12. The value of squareness (S), and anisotropy constant (K) mentioned in Table 5 were estimated using the Eqs. (22) and (23) mentioned below [61]:

$$K = \frac{H_c M_{max}}{0.96} \tag{22}$$

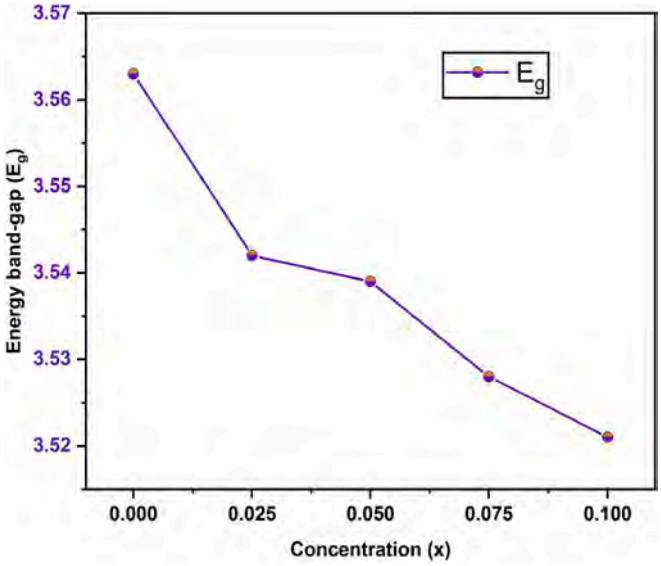

Fig.10. Variation of Energy bandgap (E_g) with the composition of MZGD ferrite NPs.

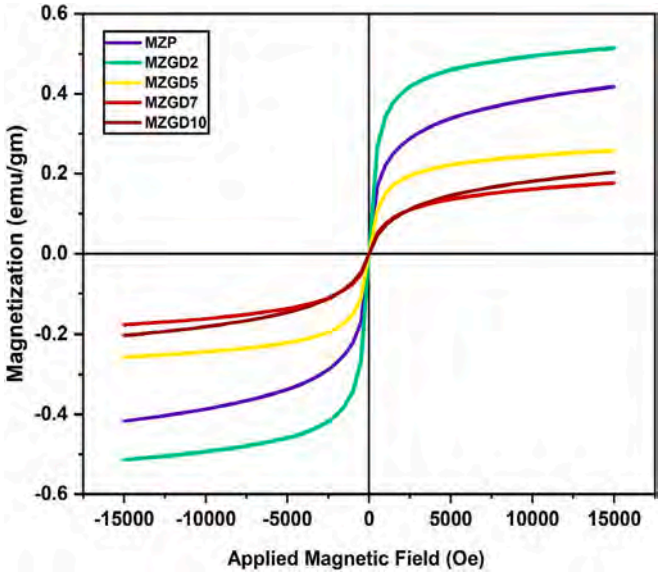

Fig.11. M–H loop for for MZP, MZGD2, MZGD5, MZGD7, and MZGD10 ferrite NPs.

Table 5
Maximum magnetization (M_{max}), Remanence magnetization (M_r) and Coercivity (H_c), Anisotropy constant (K), Squareness (S), and Magnetic moment (μ_B) for MZGD ferrite NPs.

Composition	H_c (Oe)	M_r (emu/g)	M_{max} (emu/g)	K (erg/cc)	S	μ_B (B.M)
MZP	10.88	0.199	21.97	249.14	0.0090	0.8670
MZGD2	5.47	0.150	25.69	146.46	0.0058	1.0263
MZGD5	5.23	0.074	16.10	87.78	0.0045	0.6545
MZGD7	1.49	0.010	11.76	18.34	0.0009	0.4804
MZGD10	0.74	0.006	18.46	14.28	0.0003	0.7763

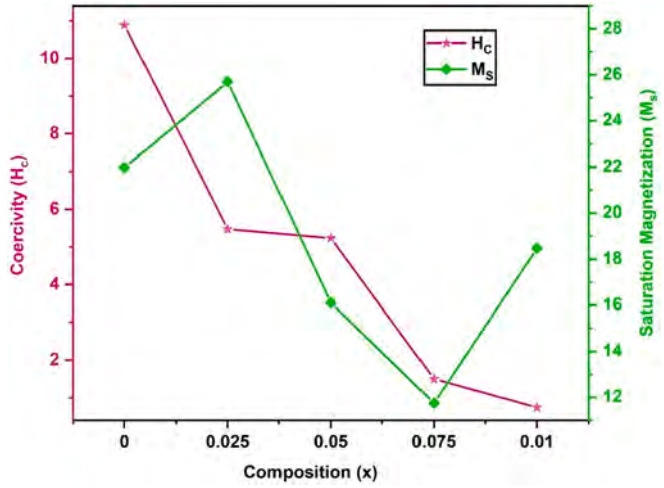

Fig.12. Variation of coercivity (H_c) and Maximum magnetization (M_{max}) with the composition of MZGD ferrite NPs.

$$S = \frac{M_R}{M_s} \tag{23}$$

'S' is a characteristic quantity for magnetic materials that also governs the presence or absence of inter-grain exchange interlinkages between the NPs.

The value of $S = 0.5$, according to Stoner and Wohlfarth, denotes non-interactive, randomly oriented particles that rotate coherently in response to the applied magnetic field. When the S is less than 0.5, the only interaction between the particles is magnetostatic. Only for S greater than 0.5 exchange coupling become apparent [62]. The squareness ratio varies from 0.009 to 0.00036. The lower value of S demonstrates that the synthesized samples have a single domain structure and that exchange interactions are reduced as a consequence of the interactions between magnetic dipoles that are randomly oriented, which also demonstrates the sample's superparamagnetic nature. Because magnetic hyperthermia is a feature of magnetic oxide NPs, when injected into tumors, it causes morphological alterations by remotely inducing heat on the application of alternating magnetic field, thereby increasing the temperature around the tissues or organs where the tumor is located resulting in reductions in the populations of both innate and adaptive immune cells. Therefore, the synthesized MZGD ferrite samples can be suitable candidates for magnetic hyperthermia applications.

3.6. Dielectric properties

The dielectric constant (ε') is also known as relative permittivity and it arises as a result of the interaction between the material and fluctuating electric field. Understanding the electrical behavior of the charge carrier's or electron movement is possible through an analysis of the dielectric characteristics. The below mentioned formula Eq. (24) is employed to estimate the dielectric constant value:

$$\varepsilon' = \frac{Cd}{A\,\varepsilon_0} \tag{24}$$

where C represents capacitance, d is the thickness, A is pellet area, and ε_o represents permittivity of vacuum. Whereas, the dielectric loss factor (ε'') determines the dissipation of energy in a dielectric material when an external electric field is applied. It can be estimated by employing the Eq. (25) mentioned below [63]:

$$\varepsilon'' = \varepsilon' tan(\delta) \tag{25}$$

here "*tan* (δ)" represents the tangent loss.

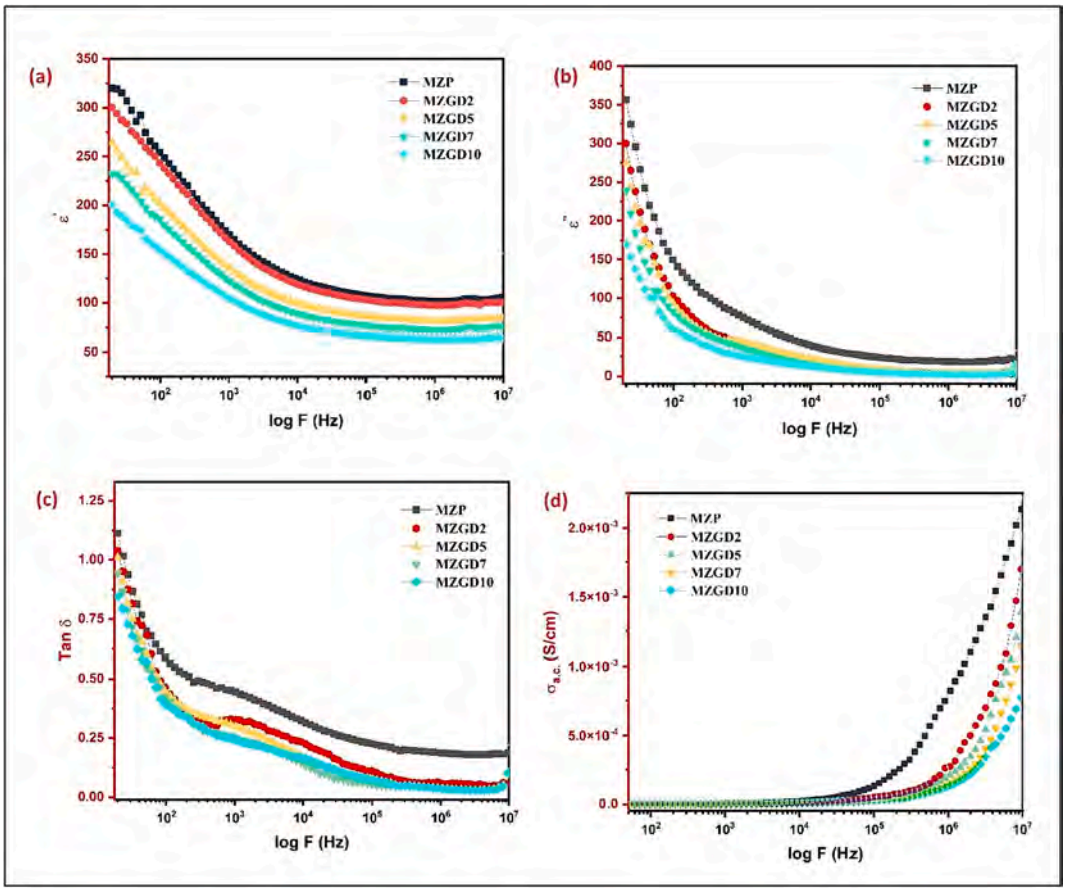

Fig.13. (a-d) Variation of ε′, ε″, tangent loss(δ), and AC conductivity v/s frequency for MZP, MZGD2, MZGD5, MZGD7, and MZGD10 ferrites NPs.

Fig. 13(a) and Fig. 13(b) illustrate the graph of the dielectric constant (ε′) and dielectric loss factor (ε″), which demonstrate that there are very small variations in ε′ and ε″ with the increasing frequency. Fig. 13(a) depicts dielectric constant of Gd^{3+} ion doped Mg-Zn nano-ferrite as a function of frequency. Up to 10^5 Hz, the magnitude of both dielectric parameters declined sharply with increasing frequency. At higher frequencies the values observed becomes nearly constant. It is determined that MZGD ferrites initially displayed high ε′ and ε'' values and declined as the frequency values increased. Similar results were reported in Gd-doped Ba-Sr Nano ferrites and Gd-doped Co-Ni cubic ferrite[64,65]. Both the Koop's theory and Maxwell-Wagner Model can be used to provide explanation for this type of behavior i.e., dielectric dispersion and resonance peaks [66].

In lower frequency region the higher value of ε' is due to the grain boundaries. At higher frequencies the grain boundaries start to conduct resulting in decrease value of ε' at higher frequency region. The aforementioned theory is supported by the space charge polarization concept, which is brought on by the electrons exchange between ions of the same element in distinct valence states at interstitial sites. When electrons hop within grains boundaries at lower frequencies, they pile up at grain boundaries, causing the polarization thus higher ε' value was observed. According to the literature, Gd^{3+} ions prefer occupying O_h position by substituting Fe^{3+} ions, thereby enhancing the concentration of Mg^{2+}/Zn^{2+} ions at grain boundaries. The process of polarization becomes more efficient at lower frequency region due to the greater concentration of the Fe^{2+} ions leading to increased values of ε′. The increased electrical resistance caused by iron ions replacement mitigates the movement of charge carriers across the grain boundaries at higher frequencies. This substantially decreases the material's dielectric characteristics by destroying the polarization build-up [67,68]. Therefore, with the increasing Gd^{3+} ion concentration, a reduction in the values of dielectric constants is observed. Whereas, the interfacial polarization and electric dipole polarization may be accountable for the resonance peaks [69]. Additionally, the resonance peaks may develop as a result of the hopping frequency being synced with the applied frequency [70]. Therefore, with the increasing Gd^{3+} ion concentration, a reduction in the values of dielectric constants is observed. Tangent loss is the ratio between the current dissipation and the fluctuating current within a material [71] and is illustrated in Fig. 13(c). The system's energy dissipation and loss in polarization are both represented by the dielectric loss tangent [72]. The relation mentioned below Eq. (26) can be utilized to estimate the tangent loss.

$$tan\,(\delta) = \frac{\varepsilon''}{\varepsilon'} \tag{26}$$

The variation in tangent loss by increasing the Gd^{3+} ion concentration is almost similar like other parameters with increasing frequency. It is apparent from Fig. 13(c) that the loss tangent tan decreases as the applied electric field frequency rises. This graph also demonstrates two regions. The values of *tan δ* exhibit an exponential decline in the first region, which extends up to 10^5 Hz. This range is followed by the second region where *tan δ* seems to be frequency-independent. Moreover, these results are supported with the findings of Gd-doped Co-Ni ferrite [65]. Because of the dispersion effect losses are higher in the lower frequency zone than in the higher frequency zone. Another significant explanation for the evident conduction losses is the increase in the concentration of dopants in place of iron. These findings support the theoretical work of Pereira [73].

Fig. 13(d) depicts the variation in the AC conductivity of MZGD ferrite NPs from 100 Hz to 100 MHz. AC electrical conductivity was estimated by the Eq. (27) mentioned below

$$\sigma_{ac} = \varepsilon' \varepsilon_o tan\delta(\omega) \quad (27)$$

Angular frequency is represented by $\omega = 2\pi f$ and frequency is denoted by f.

The values have remained nearly uniform in the lower frequency region from 10 Hz to 10 kHz. This may be due to the less hopping rate of ions. Grain boundaries prevented charge carriers from obtaining desired energy to jump between interstitial sites. AC conductivity measurements show strong and exponential growth as frequency is raised from > 10 kHz. Cause for this hike may be the dispersion effect along with the relaxation and reorientation phenomena [74]. The values of MZGD samples are higher than the pure sample indicating doped samples behaving as semiconductors and comparable results have been communicated in the literature in which they doped Gd in Co-Ni ferrite [65].

4. Conclusion

In the present work, the Gd^{3+} ion-doped Mg–Zn ferrites NPs were successfully prepared in five distinctive concentrations via co-precipitation methodology. The impact of Gd^{3+} ion doping on structural, optical, magnetic and dielectric properties was investigated. XRD investigation revealed the formation of single-phase cubic spinel structure for all compositions, with lattice parameter values between 8.35 Å and 8.37 Å and crystallite size between 7 and 13 nm. Morphological study using HR-TEM analysis reveals the spherical structure and the agglomeration of nanoparticles. Tauc's plot was used to estimate energy bandgap (E_g) values of Gd^{3+} ion doped Mg-Zn ferrites. With increasing Gd^{3+} ion concentration E_g values significantly decreased from 3.563 eV to 3.521 eV. Magnetic parameters obtained using VSM revealed the super-paramagnetic nature of synthesized samples. The magnetic properties showed an extreme dependency with the change of Gd^{3+} ion concentration. The superparamagnetic MZGD ferrite particles have the potential to be used in ferrofluids and magnetic hyperthermia since they can become magnetically activated and align with the field direction - when under the influence of an external magnetic field. The dielectric characteristics of synthesized MZGD ferrite nanoparticles were analyzed in the range of 100 Hz to 100 MHz All the dielectric parameters i.e., dielectric constant (ε'), dielectric loss (ε''), and the loss tangent (tan δ) were observed to decrease sharply with an increasing frequency and also by Gd^{3+} ion substitution. AC conductivity measurements show strong and exponential growth as frequency is raised from > 10 kHz. Reasons for this rise may be the dispersion effect along with the relaxation and reorientation phenomena. The findings discussed here are helpful for supporting the fact that how Gd^{3+} ion doping affects the transport characteristics of Mg-Zn ferrites and offer applications in electrical systems, such as semiconductor devices and electromagnetic devices that operate at high frequencies.

CRediT authorship contribution statement

Priya Boora: Writing – review & editing, Writing – original draft, Visualization, Software, Methodology, Investigation, Conceptualization. **Rohit Ranga:** Writing – original draft, Visualization, Software, Methodology, Investigation, Formal analysis, Conceptualization. **Pallavi Saini:** Writing – original draft, Visualization, Software, Methodology, Investigation, Conceptualization. **Vasundhara Madaan:** Writing – review & editing. **Permender Singh:** Writing – review & editing. **Krishan Kumar:** Writing – review & editing, Supervision, Formal analysis, Conceptualization. **Ashok Kumar:** Writing – review & editing, Visualization, Investigation, Formal analysis.

Declaration of competing interest

The authors declare that they have no known competing financial interests or personal relationships that could have appeared to influence the work reported in this paper.

Data availability

Data will be made available on request.

Acknowledgement

The authors Pallavi and Priya Boora would like to acknowledge the Department of Chemistry, DCRUST, Murthal for providing research facilities and support given during this work.

References

[1] F.A. Sheikh, H.M.N.K. Asghar, M. Khalid, Z.A. Gilani, S.M. Ali, N-ul-H. Khan, M. A. Shar, M.Y. Khan, Magnetically tuned $Ni_{0.3}Co_{0.7}Dy_xFe_{2-x}O_4$ ferrites for high-density data storage applications, App. Phys. a. 130 (65) (2024), https://doi.org/10.1007/s00339-023-07224-6.

[2] K.B. Gaikwad, K.P. Gattu, C.V. More, P.P. Pawar, Physical, structural and nuclear radiation shielding behaviour of Ni-Cu-Zn Fe_2O_4 ferrite nanoparticles, Appl. Radiation and Isotopes 207 (2024) 111244, https://doi.org/10.1016/j.apradiso.2024.111244.

[3] A. Vempaty, M. Sahni, C. Pandit, S. Pandit, A.S. Muthuriya, S. Chauhan, M. Singh, P. Vyas, Bismuth ferrite Nanoparticles-blended Carbon soot-based cathode for enhanced power production in microbial fuel cell, J. Electron. Mater. 53 (2024) 106–120, https://doi.org/10.1007/s11664-023-10757-4.

[4] R. Ranga, A. Kumar, P. Kumari, P. Singh, V. Madaan, K. Kumar, Ferrite application as an electrochemical sensor: a review, Mater Char. 178 (2021) 111269, https://doi.org/10.1016/j.matchar.2021.111269.

[5] S. Sudarsan, M. Anandkumar, E.A. Trofimov, Synthesis and characterization of copper ferrite nanocomposite from discarded printed circuit boards as an effective photocatalyst for Congo red dye degradation, J. Indust. Eng. Chem. 131 (2024) 208–220, https://doi.org/10.1016/j.jiec.2023.10.020.

[6] J.S. Ghodake, R.C. Kambale, T.J. Shinde, P.K. Maskar, S.S. Suryavanshi, Magnetic and microwave absorbing properties of Co^{2+} substituted nickel–zinc ferrites with the emphasis on initial permeability studies, J. Magn. Magn. Mater. 401 (2016) 938–942, https://doi.org/10.1016/j.jmmm.2015.11.009.

[7] A. Hebbaz, M. Belhani, T. Tahraoui, Synthesis of cerium-doped magnesium spinel ferrites and study of their physical properties for photocatalytic applications under sunlight irradiation, App. Phys. A 130 (94) (2024), https://doi.org/10.1007/s00339-023-07219-3.

[8] K. Vani, N.H. Kumar, D. Ravinder, Rare earth Gd^{3+} substituted on cobalt ferrites: structural and dielectric studies by citrate gel autocombustion method, Inorg. Chem. Commun. 160 (2024) 111920.

[9] R. Ranga, K. Kumar, A. Kumar, Influence of Ce^{3+} ion doping on structural, morphological, magnetic, dielectric and optical properties of $Mg_{0.5}Ni_{0.5}Fe_{2-x}Ce_xO_4$ ($0 \leq x \leq 0.1$) ferrite nanoparticles synthesized via coprecipitation method, J. Magn. Magn. Mater. 588 (2023) 171496, https://doi.org/10.1016/j.jmmm.2023.171496.

[10] R. Verma, S.N. Kane, P. Tiwari, F. Mazaleyrat, Cd content dependent structural and magnetic properties of Cd-Ni nano ferrite, AIP Conf. Proceed. 2142 (2019) 160001, https://doi.org/10.1063/1.5122582.

[11] S.N. Pund, P.A. Nagwade, A.V. Nagawade, A.V. Bagade, Influence of Cu^{2+} substitution on structural and optical properties of Mg-Zn ferrite nanoparticles, Mater. Today Proc. 49 (2022) 2382–2391, https://doi.org/10.1016/j.matpr.2021.09.402.

[12] S.B. Singh, C. Srinivas, B.V. Tirupanyam, C.L. Prajapat, M.R. Singh, S.S. Meena, P. Bhatt, S.M. Yusuf, D.L. Sastry, Structural, thermal and magnetic studies of $Mg_xZn_{1-x}Fe_2O_4$ nanoferrites: study of exchange interactions on magnetic anisotropy, Ceram. Int. 42 (16) (2016) 19179–19186, https://doi.org/10.1016/j.ceramint.2016.09.081.

[13] D.S. Mathew, R.-S. Juang, An overview of the structure and magnetism of spinel ferrite nanoparticles and their synthesis in microemulsions, Chem. Eng. J. 129 (1–3) (2007) 51–65, https://doi.org/10.1016/j.cej.2006.11.001.

[14] Y. Slimania, B. Unalb, M.A. Almessierea, A. Demir Korkmazc, S.E. Shirsathd, G. Yasine, A.V. Trukhanovf, Investigation of structural and physical properties of Eu^{3+} ions substituted $Ni_{0.4}Cu_{0.2}Zn_{0.4}Fe_2O_4$ spinel ferrite nanoparticles prepared via sonochemical approach a Baykal, Res. Phys. 17 (2020) 103061, https://doi.org/10.1016/j.rinp.2020.103061.

[15] R. Zhang, L. Sun, Z. Wang, W. Hao, E. Cao, Y. Zhang, Dielectric and magnetic properties of $CoFe_2O_4$ prepared by sol-gel auto-combustion method mater, Res. Bull. 98 (2018) 133–138, https://doi.org/10.1016/j.materresbull.2017.08.006.

[16] M.H. Abdellatif, G.M. El-Komy, A.A. Azab, Magnetic characterization of rare earth doped spinel ferrite, J. Magn. Magn. Mater. 442 (2017) 445–452, https://doi.org/10.1016/j.jmmm.2017.07.020.

[17] M.H. Abdellatif, A.A. Azab, M. Salerno, Effect of rare earth doping on the vibrational spectra of spinel Mn-Cr ferrite, Mater. Res. Bull. 97 (2018) 260–264, https://doi.org/10.1016/j.materresbull.2017.09.012.

[18] M.A. Almessiere, Y. Slimani, M. Sertkol, H. Gungunes, Y.S. Wudil, A.D. Korkmaz, A. Baykal, Impact of Gd substitution on the structure, hyperfine interactions, and magnetic properties of Sr hexaferrites, Ceram. Int. 47 (23) (2021) 33853–33864, https://doi.org/10.1016/j.ceramint.2021.08.297.

[19] N. Rezlescu, E. Rezlescu, C. Pasnicu, M. L. Craus, Effects of the rare-earth ions on some properties of a nickel-zinc ferrite, J. Phys.: Condens. Matter, 6(29) (1994) 5707–5716. doi: 10.1088/0953-8984/6/29/013.

[20] M. Yousaf, S. Nazir, M. Akbar, M.N. Akhtar, A. Noor, E. Hu, M.A.K.Y. Shah, Y. Lu, Structural, magnetic, and electrical evaluations of rare earth Gd^{3+} doped in mixed Co–Mn spinel ferrite nanoparticles, Ceram. Int. 48 (1) (2022) 578–586, https://doi.org/10.1016/j.ceramint.2021.09.136.

[21] N.P. Kumar, A. Chelvane, M.M. Raja, P. Sowjanya, Structural and magnetic behaviour of sol-gel prepared $Ni_{0.5}Co_{0.5}Gd_{0.025}Tb_{0.025}Dy_{0.025}Ho_{0.025}Fe_{1.99}O_4$ for energy harvesting applications, Mater. Lett. 26 (2024) 136056, https://doi.org/10.1016/j.matlet.2024.136056.

[22] K.P. Hazarika, J.P. Borah, Role of site selective, substitution, magnetic parameter tuning, and self heating in magnetite hyperthermia application: Eu0doped magnetite nanoparticles, RSC Adv. 13 (2023) 5045–5057, https://doi.org/10.1039/D2RA07924K.

[23] K. Sakthipandi, K. Venkatesan, R. Sivakumar, G. Rajkumar, B.G. Babu, S. Arunmetha, A. Hossain, M.S. Raghavan, V. Rajendran, Exploring the impact of rare-earth (La^{3+}) ion dopingo on structural, magnetic and dielectric properties of $Co_{0.50}Ni_{0.50}La_xFe_{2-x}O_4$ nano-spinel ferrite, J. Alloys Compd. 981 (2024) 173708, https://doi.org/10.1016/j.jallcom.2024.173708.

[24] B. Baburao, N.H. Kumar, A. Edukondalu, D. Ravinder, Structural, dielectric, thermoelectric, and magnatic properties of Er^{3+} ion substituted Mg-Zn spinal nanoferrites: high charge-storage capacitors and high frequency microwave device applications, Mater. Sci. Eng. b. 299 (2024) 116985, https://doi.org/10.1016/j.mseb.2023.116985.

[25] P. Jinka, S. Yalagala, K. Laxminarayana, J. Bhemaraham, M. Prasad, V. Nathanial, Structural, electrical, magnetic and anti-cancer properties of Gd-doped Mg-Cd ferrites, Hybrid Adv. 5 (2024) 100163, https://doi.org/10.1016/j.hybadv.2024.100163.

[26] M.V.S. Kumar, G.J. Shankarmurthy, E. Melagiriyappa, K.K. Nagaraja, H. S. Jayanna, M.P. Telenkov, Induced effects of Zn+2 on the transport and complex impedance properties of gadolinium substituted nickel-zinc nano ferrites, J. Magn. Magn. Mater. 478 (2019) 12–19, https://doi.org/10.1016/j.jmmm.2019.01.058.

[27] K. Vani, N.H. Kumar, D. Ravinder, Rare earth Gd^{3+} substituted on cobalt ferrites: structural and dielectric studies by citrate gel auto-combustion method, Inorg. Chem. Commun. 160 (2024) 111920, https://doi.org/10.1016/j.inoche.2023.111920.

[28] A.J. Giustini, A.A. Petryk, S.M. Cassim, J.A. Tate, I. Baker, P.J. Hoopes, Magnetic nanoparticle hyperthermia in cancer treatment, Nano LIFE. 01 (2010) 17–32, https://doi.org/10.1142/S1793984410000067.

[29] A.L. Elrefai, T. Yoshida, K. Enpuku, Magnetic parameters evaluation of magnetic nanoparticles for use in biomedical applications, J. Magn. Magn. Mater. 474 (2019) 522–527, https://doi.org/10.1016/j.jmmm.2018.11.022.

[30] F. Hirosawa, T. Iwasaki, Synthesis and magnetic induction heating properties of Gd-substituted Mg–Zn ferrite nanoparticles, S. Watano, Appl. Nanosci. 7(5) (2017) 209–214. doi: 10.1007/s13204-017-0566-y.

[31] S. Rahman, K. Nadeem, M.A. Rehman, M. Mumtaz, S. Naeem, I.L. Papst, Structural and magnetic properties of ZnMg-ferrite nanoparticles prepared using the co-precipitation method, Ceram. Int. 39 (5) (2013) 5235–5239, https://doi.org/10.1016/j.ceramint.2012.12.023.

[32] S.B. Somvanshi, S.A. Jadhav, M.V. Khedkar, P.B. Kharat, S.D. More, K.M. Jadhav, Structural, thermal, spectral, optical and surface analysis of rare earth metal ion (Gd3+) doped mixed Zn–Mg nano-spinel ferrites, Ceram. Int. 46 (9) (2020) 13170–13179, https://doi.org/10.1016/j.ceramint.2020.02.091.

[33] S. Torkian, A. Ghasemi, R. S. Razavi, Structural and Magnetic Consequences of $Mn_{0.6}Zn_{0.4}Fe_{2-x}Gd_xO_4$ Ferrite, J. Supercond. Nov. Magn. 29(6) (2016) 1617–1625. doi: 10.1007/s10948-016-3458-6.

[34] S.S. Hasolkar, P.P. Naik, Effect of Gd^{+3} doping on structural, magnetic and electrical properties of $Mn_{0.5}Co_{0.5}Fe_{2-x}Gd_xO_4$ nano-particles prepared using combustion synthesis, J. Alloys Compd. 823 (2020) 153605, https://doi.org/10.1016/j.jallcom.2019.153605.

[35] R. P. Pant, M. Arora, B. Kaur, V. Kumar, A. Kumar, Finite size effect on Gd^{3+} doped $CoGd_xFe_{2-x}O_4$ ($0.0 \leq x \leq 0.5$) particles, J. Magn. Magn. Mater. 322(22) (2010) 3688–3691. doi: 10.1016/j.jmmm.2010.07.026.

[36] A. M. Wahba, B. E. M. Moharam, The impact of cation distribution on the structural and magnetic properties of nonstoichiometric $Co_{0.5}Ni_{0.5+x}Fe_{2-x}O_4$ nanoferrites, A. F. Mahmoud, J. Mater. Sci.: Mater. Electron. 32(11) (2021) 14194–14206. doi: 10.1007/s10854-021-05978-4.

[37] T.J. Shinde, A.B. Gadkari, P.N. Vasambekar, Influence of Nd^{3+} substitution on structural, electrical and magnetic properties of nanocrystalline nickel ferrites, J. Alloys Compd. 513 (2012) 80–85, https://doi.org/10.1016/j.jallcom.2011.10.001.

[38] S.F. Mansour, N.G. Imam, S. Goda, M.A. Abdo, Constructive coupling between $BiFeO_3$ and $CoFe_2O_4$; promising magnetic and dielectric properties, J. Mater. Res. Technol. 9 (2) (2020) 1434–1446, https://doi.org/10.1016/j.jmrt.2019.11.069.

[39] S. Kumari, P. Thakur, S. Singh, A. Thakur, A detailed structural analysis, morphological and optical study of Mg-Zn nano ferrite, Mater. Today Proceed. 73 (2) (2022) 233–236, https://doi.org/10.1016/j.matpr.2022.07.201.

[40] R. Ranga, K. Kumar, A. Kumar, Morphology, structural, dielectric and magnetic study of Ce^{3+} ion doped $Mg_{0.5}Zn_{0.5}Fe_{2-x}Ce_xO_4$ ($0.0 \leq x \leq 0.1$) ferrite nanoparticles mater, Chem. Phys. 289 (2022) 126482, https://doi.org/10.1016/j.matchemphys.2022.126482.

[41] J. Lin, Y. He, X. Du, Q. Lin, H. Yang, H. Shen, Structural and magnetic studies of Cr^{3+} substituted nickel ferrite nanomaterials Prepared by Sol-Gel auto-combustion, Cryst. (basel) 8 (10) (2018) 384, https://doi.org/10.3390/cryst8100384.

[42] Somnath, et al., Structural, magnetic and mössbauer studies of Nd-doped Mg-Mn ferrite nanoparticles, J. Magn. Magn. Mater. 444 (2017) 77–86, https://doi.org/10.1016/j.jmmm.2017.08.017.

[43] Z.C. Zhong, L.Z. Li, X.H. Wu, X.X. Zhong, Z.X. Tao, H.S. Guo, F.H. Wang, T. Wang, Influence of Nd substitution on the structural, magnetic and electrical properties of NiZnCo ferrites, Ceram. Int. 47 (7) (2021) 8781–8786, https://doi.org/10.1016/j.ceramint.2020.11.243.

[44] M.F. Al-Hilli, S. Li, K.S. Kassim, Structural analysis, magnetic and electrical properties of samarium substituted lithium–nickel mixed ferrites, J. Magn. Magn. Mater. 324 (5) (2012) 873–879, https://doi.org/10.1016/j.jmmm.2011.10.005.

[45] V. Chaudhari, S.E. Shirsath, M.L. Mane, R.H. Kadam, S.B. Shelke, D.R. Mane, Crystallographic, magnetic and electrical properties of $Ni_{0.5}Cu_{0.25}Zn_{0.25}La_xFe_{2-x}O_4$ nanoparticles fabricated by sol–gel method, J. Alloys Compd. 549 (2013) 213–220, https://doi.org/10.1016/j.jallcom.2012.09.060.

[46] R. Ranga, K. Kumar, A. Kumar, Morphology, structural and magnetic study of superparamagnetic $Mg_{0.5}Zn_{0.5}Fe_{2-x}La_xO_4$ ($0 \leq x \leq 0.1$) ferrite nanoparticles synthesized by chemical coprecipitation method, Ceram. Int. 49(2) (2023) 2956–2966. doi: 10.1016/j.ceramint.2022.09.280.

[47] C.O. Arean, E.G. Diaz, J.M.R. Gonzalez, M.A.V. Garcia, Crystal chemistry of cadmium-zinc ferrites, J. Solid State Chem. 77 (2) (1988) 275–280, https://doi.org/10.1016/0022-4596(88)90249-6.

[48] M.N. Akhtar, M.A. Khan, Effect of rare earth doping on the structural and magnetic features of nanocrystalline spinel ferrites prepared via sol gel route, J. Magn. Magn. Mater. 460 (2018) 268–277, https://doi.org/10.1016/j.jmmm.2018.03.069.

[49] R.D. Waldron, Infrared spectra of ferrites, Phys. Rev. 99 (6) (1955) 1727–1735, https://doi.org/10.1103/PhysRev.99.1727.

[50] K.B. Modi, M.K. Rangolia, M.C. Chhantbar, H.H. Joshi, J. Mater. Sci. 41 (22) (2006) 7308–7318, https://doi.org/10.1007/s10853-006-0929-3.

[51] R. Tholkappiyan, K. Vishista, Combustion synthesis of Mg–Er ferrite nanoparticles: cation distribution and structural, optical, and magnetic properties, Mater. Sci. Semicond. Process. 40 (2015) 631–642, https://doi.org/10.1016/j.mssp.2015.06.076.

[52] D.R. Kumar, S.I. Ahmad, C.A. Lincoln, D. Ravinder, Structural, optical, room-temperature and low-temperature magnetic properties of Mg–Zn nanoferrite ceramics, J. Asian Ceram. Soc. 7 (1) (2019) 53–68, https://doi.org/10.1080/21870764.2018.1563036.

[53] R. P. Pant, M. Arora, B. Kaur, V. Kumar, A. Kumar, Finite size effect on Gd^{3+} doped $CoGd_xFe_{2-x}O_4$($0.0 \leq x \leq 0.5$) particles, J. Magn. Magn. Mater. 322(22) (2010) 3688–3691. doi: 10.1016/j.jmmm.2010.07.026.

[54] S. Thota, S.C. Kashyap, S.K. Sharma, V.R. Reddy, Micro raman, mossbauer and magnetic studies of manganese substituted zinc ferrite nanoparticles: role of Mn, J. Phys. Chem. Solids. 91 (2016) 136–144, https://doi.org/10.1016/j.jpcs.2015.12.013.

[55] S.B. Patil, H.S. Bhojya Naik, G. Nagaraju, R. Viswanath, S.K. Rashmi, Synthesis of visible light active Gd^{3+}-substituted $ZnFe_2O_4$ nanoparticles for photocatalytic and antibacterial activities, The European Phys. J. plus. 132 (8) (2017) 328, https://doi.org/10.1140/epjp/i2017-11602-x.

[56] A. Manikandan, J.J. Vijaya, M. Sundararajan, C. Meganathan, L.J. Kennedy, M. Bououdina, Optical and magnetic properties of Mg-doped ZnFe2O4 nanoparticles prepared by rapid microwave combustion method, Superlattices Microstruct. 64 (2013) 118–131, https://doi.org/10.1016/j.spmi.2013.09.021.

[57] A. Meidanchi, H. Ansari, Copper spinel ferrite Superparamagnetic Nanoparticles as a novel radiotherapy enhancer effect in cancer treatment, J. Clust. Sci. 32 (3) (2021) 657–663, https://doi.org/10.1007/s10876-020-01832-5.

[58] L. Zhao, Y. Cui, H. Yang, L. Yu, W. Jin, S. Feng, The magnetic properties of $Ni_{0.7}Mn_{0.3}Gd_xFe_{2-x}O_4$ ferrite, Mater. Lett. 60(1) (2006) 104–108. doi: 10.1016/j.matlet.2005.07.083.

[59] X.C. Zhong, X.J. Guo, S.Y. Zou, H.Y. Yu, Z.W. Liu, Y.F. Zhang, K.X. Wang, Improving soft magnetic properties of Mn-Zn ferrite by rare earth ions doping, AIP Adv. 8 (4) (2018) 047807, https://doi.org/10.1063/1.4993645.

[60] R. Ranga, K. Kumar, A. Kumar, Influence of rare-earth La^{3+} ion doping on microstructural, magnetic and dielectric properties of $Mg_{0.5}Ni_{0.5}Fe_{2-x}La_xO_4$ ($0 \leq x \leq 0.1$) ferrite nanoparticles, Mater. Ceram. Int. 49 (2023) 33333–33350, https://doi.org/10.1016/j.ceramint.2023.08.048.

[61] R. Ranga, K. Kumar, A. Kumar, Cerium doped Mg–Co mixed ferrite nanoparticles; synthesis, magnetic and dielectric study, J. Mater. Sci.: Mater. Electron. 34 (2023) 1931, https://doi.org/10.1007/s10854-023-11305-w.

[62] L. Phor, S. Chahal, V. Kumar, Zn2+ substituted superparamagnetic MgFe2O4 spinel-ferrites: investigations on structural and spin-interactions, J. Adv. Ceram. 9 (5) (2020) 576–587, https://doi.org/10.1007/s40145-020-0396-3.

[63] A. Majeed, M.A. Khan, F.U. Raheem, I. Ahmad, M.N. Akhtar, M.F. Warsi, Morphological, raman, electrical and dielectric properties of rare earth doped X-type hexagonal ferrites, Physica B Condens. Matter. 503 (2016) 38–43, https://doi.org/10.1016/j.physb.2016.08.041.

[64] A. Liaquat, M.A.U. Rehman, A.U. Haq, Impact of Gd doping on the dielectric and magnetic properties of (Sr–Ba)Fe12O19 nanoparticles, J. Alloys Compd. 822 (2020) 153561, https://doi.org/10.1016/j.jallcom.2019.153561.

[65] A. Ditta, M.A. Khan, M. Junaid, R.M.A. Khalil, M.F. Warsi, Structural, magnetic and spectral properties of Gd and Dy co-doped dielectrically modified Co-Ni ($Ni_{0.4}Co_{0.6}Fe_2O_4$) ferrites, Physica B Condens. Matter. 507 (2017) 27–34, https://doi.org/10.1016/j.physb.2016.11.030.

[66] M.J. Iqbal, S. Farooq, Could binary mixture of Nd–Ni ions control the electrical behavior of strontium–barium M-type hexaferrite nanoparticles, Mater. Res. Bull. 46 (5) (2011) 662–667, https://doi.org/10.1016/j.materresbull.2011.01.025.

[67] T.T. Carol, J. Mohammed, A.K. Srivastava, Effect of calcination temperature on the structural, dielectric and optical properties of nano-sized M-type barium

hexaferrites, Mater. Today Proc. 18 (2019) 566–574, https://doi.org/10.1016/j.matpr.2019.06.449.
[68] K. Iwauchi, Dielectric properties of fine Particles of Fe3O4 and some ferrites, Jpn. J. Appl. Phys. 10 (11) (1971) 1520, https://doi.org/10.1143/JJAP.10.1520.
[69] Z. Haijun, Y. Xi, Z. Liangying, The preparation and microwave properties of $Ba_2Zn_xCo_{2-x}Fe_{28}O_{46}$ hexaferrites, J. Magn. Magn. Mater. 241 (2–3) (2002) 441–446, https://doi.org/10.1016/S0304-8853(01)00447-4.
[70] M.N. Ashiq, S. Shakoor, M. Najam-ul-Haq, M.F. Warsi, I. Ali, I. Shakir, J. Magn. Magn. Mater. 374 (2015) 173–178, https://doi.org/10.1016/j.jmmm.2014.08.020.
[71] A. Majeed, M.A. Khan, F. Ur Raheem, I. Ahmad, M.N. Akhtar, M.F. Warsi, Morphological, raman, electrical and dielectric properties of rare earth doped X-type hexagonal ferrites, Physica B Condens. Matter. 503 (2016) 38–43, https://doi.org/10.1016/j.physb.2016.08.041.
[72] K. Tanbir, M. P. Ghosh, R. K. Singh, S. Mukherjee, Gd-doped soft Mn–Zn nanoferrites: synthesis, microstructural, magnetic and dielectric characterizations, J. Mater. Sci.: Mater. Electron. 31(4) (2020) 3529–3538. doi: 10.1007/s10854-020-02901-1.
[73] F. M. M. Pereira et al. Structural, magnetic and spectral properties of Gd and Dy co-doped dielectrically modified Co-Ni ($Ni_{0.4}Co_{0.6}Fe_2O_4$) ferrites, J. Mater. Sci.: Mater. Electron. 20(5) (2009) 408–417. doi: 10.1007/s10854-008-9744-8.
[74] M. A. Rehman et al., Study of dielectric relaxations in co-precipitated Sr–Fe(Cr) nanoferrites, J. Mater. Sci.: Mater. Electron., 26 (9) (2015) 6539–6545. doi: 10.1007/s10854-015-3250-6.